

Complete All-Optical Quantum Control of Electron Spins in InAs/GaAs Quantum Dot Molecule

Guy Z. Cohen

Department of Physics, University of California, San Diego, La Jolla, California 92093-0319
(Dated: August 30, 2021)

The spin states of electrons and holes confined in InAs quantum dot molecules have recently come to fore as a promising system for the storage or manipulation of quantum information. We describe here a feasible scheme for complete quantum optical control of two electron spin qubits in two vertically-stacked singly-charged InAs quantum dots coupled by coherent electron tunneling. With an applied magnetic field transverse to the growth direction, we construct a universal set of gates that corresponds to the possible Raman transitions between the spin states. We detail the procedure to decompose a given two-qubit unitary operation, so as to realize it with a successive application of up to 8 of these gates. We give the pulse shapes for the laser pulses used to implement this universal set of gates and demonstrate the realization of the two-qubit quantum Fourier transform with fidelity of 0.881 and duration of 414 ps. Our proposal therefore offers an accessible path to universal computation in quantum dot molecules and points to the advantages of using pulse shaping in coherent manipulation of optically active quantum dots to mitigate the negative effects of unintended dynamics and spontaneous emission.

I. INTRODUCTION

Spins in semiconductor quantum dots^{1,2} (QD) are promising candidates for satisfying the DiVincenzo criteria for quantum computation,³ such as state initialization,⁴⁻⁷ coherent spin manipulation,^{8,9} and qubit-specific measurements.^{10,11} The advantages of QD spin qubits over other qubit realizations are numerous. Quantum dots are compatible with existing semiconductor technology and can be grown in millions in a regular 2D array on a single millimeter-sized chip.¹² QD spin qubits can be integrated on a chip with photonic crystal cavities,¹³⁻¹⁵ have short optical recombination and photon emission times,^{16,17} can be manipulated by fast single-qubit^{8,18,19} and two-qubit^{20,21} quantum gates, and can be entangled with adjacent qubits by tunneling interaction²² or with remote ones via entanglement swapping with photons.²³⁻²⁵ Recently, great progress was made in developing methods to increase the QD spin decoherence time either through spin echo²⁶ or suppression of nuclear-spin fluctuations.²⁷

The study of the interaction mechanisms between QDs can lead to finding new ways to successfully manipulate their quantum state, an important goal of quantum information technologies, like quantum computing and quantum cryptography. Such coupling can be obtained in optically active self-assembled QDs,^{28,29} with techniques existing for ultrafast laser initialization,³⁰ measurement^{11,30} and coherent manipulation^{20,22,31-33} of the spin qubits in these QDs. Many coupling mechanisms of optically active QDs were studied including electron tunneling,^{22,32} hole tunneling,^{20,34} exciton-mediated interaction³¹ and electron-hole exchange interaction.³³ In particular, it was found that embedding two coupled QDs, which form a QD molecule (QDM), in a Schottky diode structure enables the tuning of the relative energy levels of the two dots.^{35,36} Like real molecules, QDMs can

display bonding and anti-bonding states, that are symmetric and anti-symmetric superpositions of localized states.²⁸ However, unlike natural diatomic molecules, which always have a bonding ground state, QDMs can be tailored to have molecular ground states with anti-bonding character.³⁷

With the QDM embedded in a Schottky diode, the tuning of the voltage bias determines the stable ground state charge configuration.²⁹ Especially important is the case of a doubly charged QDM,^{20,22,31,33} where each of the QDs is charged with a single electron or hole, since then the QDM can be used as a double spin qubit system. An ambitious goal in quantum computation is complete quantum control of such a multiple-qubit system. This control can be achieved by a universal set of quantum gates, i.e. a set of gates with which an arbitrary unitary operation can be constructed. Many universal sets of quantum gates were proposed. Ref. 38 showed the set of all two-level unitary gates is universal. Then, Ref. 39 showed this set of gates can be implemented by combinations of single-qubit gates and the two-qubit controlled-NOT (CNOT) gates. Other universal sets consisting of only two-qubit gates were also found.⁴⁰⁻⁴³

In this work, we present a scheme for complete quantum control of a two-qubit system, a QDM composed of two vertically-stacked singly-charged InAs QDs separated by a GaAs/AlGaAs tunnel barrier and embedded in a Schottky diode. The two electrons interact by kinetic exchange, which is based on coherent electron tunneling and evidenced by a singlet-triplet splitting of the QDM energy levels. Quantum optical control is realized through real or virtual excitation of the bottom QD electron by laser pulses. The universal set of gates consists of the 5 two-level unitary operations that correspond to the possible Raman transitions in the Voigt geometry. We find that every two-qubit unitary operation can be realized through at most 8 such Raman transitions, and

that pulse shaping the laser pulses can substantially increase the fidelity of the operation. As a case in point, we show a reasonably high fidelity realization of the two-qubit quantum Fourier transform (QFT) in this system taking light hole mixing, decay and decoherence into account. The results indicate the promise of QDMs as a platform for quantum computation and the potential of pulse shaping for increasing the fidelity of quantum state manipulation in optically active QDs.

The paper is organized as follows. In Sec. II we present the system model and Hamiltonian. We write the Hamiltonian relative to an orthogonal basis, find the eigenstates and eigenenergies, and plot the allowed transitions in the Faraday and Voigt geometries. In Sec. III we describe a universal set of gates for the QDM. We give an algorithm for decomposing a given arbitrary two-qubit unitary operation to a product of operations realized with these gates and give criteria for a subset of these gates to still be universal. In Sec. IV we present the Hamiltonian of the interaction with the electromagnetic field and discuss the pulse shapes used to implement Raman transitions and the effects of light hole mixing. In Sec. V we consider the effect of decay and decoherence. We write the Lindblad equation for the system and derive the expression for the fidelity of an operation relative to an ideal one. In Sec. VI we show, for realistic parameters, how to apply the scheme to realize the two-qubit QFT with reasonably high fidelity. Finally, in Sec. VII we discuss the key results and consider directions for future research.

II. SYSTEM MODEL AND HAMILTONIAN

The system under consideration consists of two InAs vertically stacked self-assembled quantum dots separated by a GaAs/AlGaAs tunnel barrier and embedded in a Schottky diode. The voltage of the diode is adjusted to the charge stability region where each dot occupied with a single electron at the ground state. The coherent tunnel coupling of the electrons in the two dots is manifested in inter-electron kinetic exchange interaction, which gives rise to singlet and triplet electron states delocalized over both dots. The quantum states of the electrons are optically manipulated via laser fields that generate real or virtual electron-hole pairs (excitons) at the bottom dot. The magnetic field is initially taken as zero.

With the growth direction taken to be in the z direction, the potential experienced by a single electron in the conduction band is given by

$$U(\mathbf{r}) = \frac{1}{2}m_{\perp}\omega_{\perp}^2(x^2 + y^2) + U(z), \quad (1)$$

where m_{\perp} is the effective electron mass in the x and y directions, approximated as independent of z , ω_{\perp} is the effective frequency of the parabolic confinement in the x and y directions, and $U(z)$ is plotted in Fig. 1. The

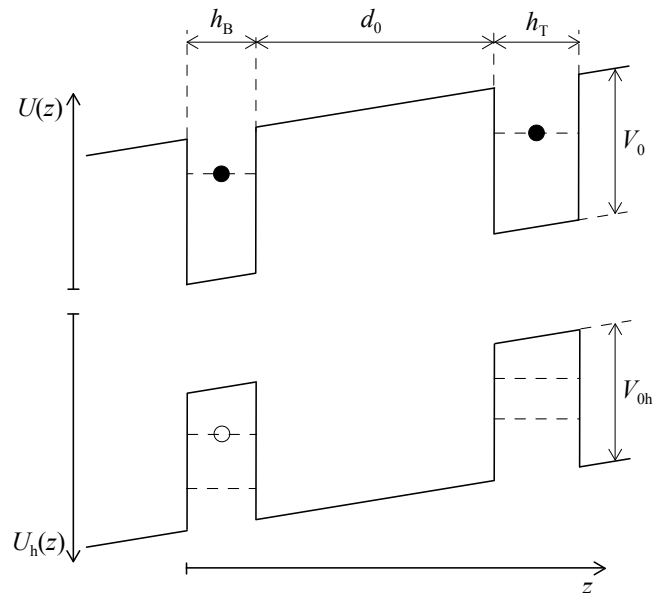


FIG. 1. Schematic diagram of the band structure of two vertically stacked self-assembled quantum dots embedded in a Schottky diode. The growth direction is the z direction. The height of the bottom/top dot is h_B/h_T , while the height of the interdot tunnel barrier is d_0 . Optical control of the two-electron spin state is achieved through real or virtual transitions to the optically excited states using laser fields tuned to create an exciton at the bottom dot only. The electric field in the z direction, F , is exaggerated for clarity.

Hamiltonian for the i th electron, in turn, reads

$$h_i = \frac{p_{i,x}^2 + p_{i,y}^2}{2m_{\perp}} + \frac{p_{i,z}^2}{2m(z_i)} + U(\mathbf{r}_i), \quad (2)$$

where \mathbf{r}_i and \mathbf{p}_i ($i = 1, 2$) are the position and momentum of the i th electron, and where the effective mass in the z direction is $m(z)$. The two-electron Hamiltonian is constructed by writing Eq. (2) for each electron and adding the Coulomb interaction term. It is

$$\mathcal{H} = h_1 + h_2 + \frac{e_0^2}{|\mathbf{r}_1 - \mathbf{r}_2|}, \quad (3)$$

where $e_0^2 \equiv e^2/(4\pi\epsilon_0)/\{\epsilon(z_1) + \epsilon(z_2)\}/2\}$, e being the electron charge, ϵ_0 the vacuum permittivity and $\epsilon(z)$ the relative dielectric constant.

We consider the two dots to be separated such as to justify a variational treatment in terms of atomic-like single-particle states localized at the individual dots. These single particle states are $|B\rangle|\uparrow\rangle$, $|B\rangle|\downarrow\rangle$, $|T\rangle|\uparrow\rangle$ and $|T\rangle|\downarrow\rangle$, where $|B\rangle/|T\rangle$ is a state corresponding to the solution of the Schrödinger equation for the single-particle Hamiltonian in Eq. (2) with $U(z)$ containing only the bottom/top dot potential well. Listing the two-electron combinations of these states gives the product state basis: $|\uparrow, \uparrow\rangle$, $|\uparrow, \downarrow\rangle$, $|\downarrow, \uparrow\rangle$, $|\downarrow, \downarrow\rangle$, $|\downarrow\uparrow, 0\rangle$ and $|0, \downarrow\uparrow\rangle$, where $|\sigma_B, \sigma_T\rangle$ is the state with the bottom/top dot occupied

by an electron with spin projection σ_B/σ_T in the z direction, 0 denotes an unoccupied dot, and $\downarrow\uparrow$ denotes a doubly-occupied dot.

With foresight, we choose a new basis composed of linear combinations of the product state basis states. The

new basis reads

$$|+\rangle = 2^{-1/2}(|\downarrow\uparrow, 0\rangle + |0, \downarrow\uparrow\rangle), \quad (4)$$

$$|S\rangle = 2^{-1/2}(|\uparrow, \downarrow\rangle - |\downarrow, \uparrow\rangle), \quad (5)$$

$$|T_0\rangle = 2^{-1/2}(|\uparrow, \downarrow\rangle + |\downarrow, \uparrow\rangle), \quad (6)$$

$$|T_+\rangle = |\uparrow, \uparrow\rangle, \quad (7)$$

$$|T_-\rangle = |\downarrow, \downarrow\rangle, \quad (8)$$

$$|-\rangle = 2^{-1/2}(|\downarrow\uparrow, 0\rangle - |0, \downarrow\uparrow\rangle), \quad (9)$$

where $|\pm\rangle$ are the symmetric/antisymmetric doubly occupied states, $|S\rangle$ and $|T_0\rangle$ are the singlet and triplet Heitler-London states, and $|T_\pm\rangle$ are the two other triplet states. The spatial parts of the triplet states are anti-symmetric, while those parts in the rest of the states are symmetric. This corresponds to the former/latter being anti-bonding/bonding states.

The Hamiltonian in Eq. (3) in the basis of Eqs. (4-9) is

$$\mathcal{H} = (\epsilon_B + \epsilon_T)\hat{I} + \begin{pmatrix} \frac{U_B+U_T}{2} + J & t_B + t_T & 0 & 0 & 0 & \epsilon_B - \epsilon_T + \frac{U_B-U_T}{2} \\ t_B + t_T & U_{BT} + J & 0 & 0 & 0 & t_B - t_T \\ 0 & 0 & U_{BT} - J & 0 & 0 & 0 \\ 0 & 0 & 0 & U_{BT} - J & 0 & 0 \\ 0 & 0 & 0 & 0 & U_{BT} - J & 0 \\ \epsilon_B - \epsilon_T + \frac{U_B-U_T}{2} & t_B - t_T & 0 & 0 & 0 & \frac{U_B+U_T}{2} - J \end{pmatrix}, \quad (10)$$

where \hat{I} is the identity matrix, and the following definitions are employed:

$$\epsilon_B = \langle B|h|B\rangle, \quad (11)$$

$$\epsilon_T = \langle T|h|T\rangle, \quad (12)$$

$$t = -\langle B|h|T\rangle, \quad (13)$$

$$t_B = t - u_{BBBT} - \langle B|T\rangle\epsilon_B, \quad (14)$$

$$t_T = t - u_{TTTB} - \langle B|T\rangle\epsilon_T, \quad (15)$$

$$J = u_{BTBT} - 2\langle B|T\rangle t. \quad (16)$$

The single-particle Hamiltonian h in Eqs. (11-13) is given in Eq. (2). The matrix elements of this Hamiltonian in Eqs. (11-12) are the single-particle energies for the states $|B\rangle$ and $|T\rangle$, apart from small contributions from the other quantum well in $U(z)$. The matrix element t in Eq. (13) is termed the tunneling matrix element. The Coulomb integral u_{ijkl} ($i, j, k, l = B$ or T) is given by

$$u_{ijkl} = \int d\mathbf{r}_1 d\mathbf{r}_2 \frac{e_0^2}{|\mathbf{r}_1 - \mathbf{r}_2|} \phi_i^*(\mathbf{r}_1) \phi_j^*(\mathbf{r}_2) \phi_k(\mathbf{r}_2) \phi_l(\mathbf{r}_1), \quad (17)$$

with $\phi_i(\mathbf{r})$ being the atomic-like single-particle wave function of the state $|i\rangle$. For the direct Coulomb integrals we use the abbreviations $U_{ij} = u_{ijji}$ and $U_i = u_{iiii}$.

We make the basis of states in Eqs. (4-9) orthogonal by replacing $|+\rangle$ and $|S\rangle$ in Eqs. (4-5) by $(|S\rangle \pm |+\rangle)$. We then normalize the states of the orthogonal basis and

write the Hamiltonian in Eq. (10) in the orthonormal basis. The diagonalization of this Hamiltonian shows the three triplet states $|T_0\rangle$, $|T_\pm\rangle$ are degenerate eigenstates with an energy independent of the electric field F . The singlet state $|S\rangle$ is shifted in energy by the kinetic exchange interaction below the triplet states, and this interaction also results in an admixture of the doubly occupied states $|\pm\rangle$ in the eigenstate dominated by $|S\rangle$. For the specific experimental values of $h_B = 2.6$ nm, $h_T = 3.2$ nm, $d_0 = 9$ nm (see Fig. 1) and $\Delta_{S-T} = 125$ μ eV, taken from Ref. 22, we plot the eigenenergies of \mathcal{H} as a function of the external electric field F in Fig. 2. The working point is taken as the one for which the singlet-triplet splitting is $\Delta_{S-T} = 125$ μ eV, and at this point the singlet eigenstate is numerically obtained as $|\tilde{S}\rangle = 0.973|S\rangle - 0.173|+\rangle + 0.149|-\rangle$. We term this state together with the triplet states, the spin states.

We now consider the optically excited states in our system, namely the X^{2-} states which consist of a negative trion at the bottom dot and an unpaired electron at the top dot. These states are $|\downarrow\uparrow\uparrow, \uparrow\rangle$, $|\downarrow\uparrow\uparrow, \downarrow\rangle$, $|\downarrow\uparrow\downarrow, \uparrow\rangle$, and $|\downarrow\uparrow\downarrow, \downarrow\rangle$, with $|\downarrow\uparrow\uparrow\rangle = 2^{-1/2}(|\uparrow\downarrow\rangle - |\downarrow\uparrow\rangle)|\uparrow\rangle$ and $|\downarrow\uparrow\downarrow\rangle = 2^{-1/2}(|\uparrow\downarrow\rangle - |\downarrow\uparrow\rangle)|\downarrow\rangle$ representing triions, and with $|\uparrow\rangle = |\frac{3}{2}, \frac{3}{2}\rangle$ and $|\downarrow\rangle = |\frac{3}{2}, -\frac{3}{2}\rangle$ being the heavy hole states with $3/2$ and $-3/2$ spin projections along z . The spin states can be excited to the optically excited states, which we term the trion states, through

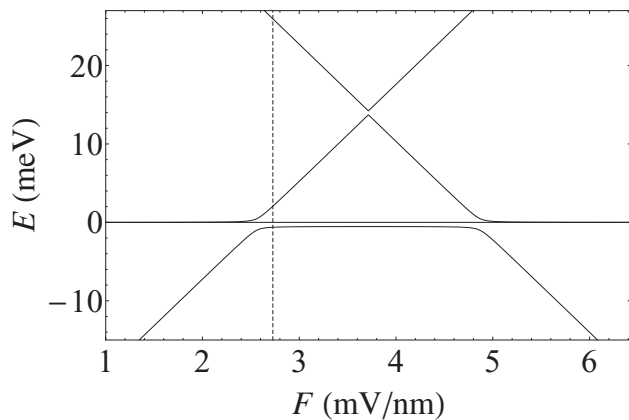


FIG. 2. Calculated spin state energy levels for the quantum dot molecule system vs. F , the applied electric field in z direction, with the experimental parameters of $h_B = 2.6$ nm, $h_T = 3.2$ nm, $d_0 = 9$ nm, $\Delta_{S-T} = 125$ μeV and zero magnetic field. The plotted energy levels at the working point ($F = 2.73$ mV/nm), denoted by a dashed line, correspond, from bottom to top, to the modified singlet state $|\tilde{S}\rangle$; the degenerate triplet states $|T_-\rangle$, $|T_0\rangle$ and $|T_+\rangle$ and two linear combinations of the two doubly occupied states $|\downarrow\uparrow, 0\rangle$ and $|0, \downarrow\uparrow\rangle$ with small (5.4% and 0.05% at the working point) singlet state admixtures. The lowest/highest energy levels were shifted down/up by 0.5 meV for the energy gaps to become visible in the plot. These energy gaps are, from top to bottom, the anticrossing splitting of the doubly occupied states which equals 35 μeV and the singlet-triplet splitting which is 35 μeV at the center of the splitting ($F = 3.71$ mV/nm) and 125 μeV at the working point.

the creation of an exciton at the bottom dot by the laser field. The 4 trion states have the same single-particle and Coulomb interaction terms in their energies. Moreover, we calculated for a wide range of relevant experimental values that the electron-hole spin exchange interaction is negligible, since the unpaired electron and hole reside in different dots. We also found that hole tunneling is too weak to have a notable effect on the energies due to the highly localized hole wave functions. We therefore conclude the trion states are degenerate.

With the energies of the spin states and the trion states determined, we obtain the selection rules and plot the energy level diagram for the system in the Faraday geometry and zero magnetic field in Fig. 3. The allowed transitions are with circularly polarized light with polarizations σ_{\pm} . We notice the $|T_{\pm}\rangle$ states are each isolated from the rest of the spin states in the sense that no Raman transition can be induced between each of these states and another spin state. This result, which persists when a magnetic field in the z direction is applied, precludes complete optical control of the two-electron spin state in this geometry and, consequently, we decide to consider the Voigt geometry with a magnetic field applied in the $+x$ direction.

The application of a magnetic field in the $+x$ direction

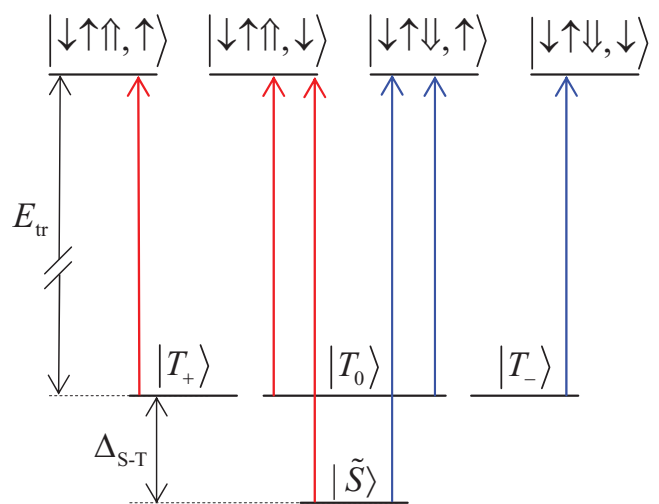


FIG. 3. (color online) Energy level diagram of the quantum dot molecule in the Faraday geometry with zero magnetic field. The states include the modified singlet state $|\tilde{S}\rangle$; the degenerate triplet states $|T_0\rangle$, $|T_+\rangle$ and $|T_-\rangle$; and the optically excited degenerate trion states $|\downarrow\uparrow\uparrow, \uparrow\rangle$, $|\downarrow\uparrow\uparrow, \downarrow\rangle$, $|\downarrow\uparrow\downarrow, \uparrow\rangle$ and $|\downarrow\uparrow\downarrow, \downarrow\rangle$ with energy E_{tr} . The kinetic exchange interaction shifts the modified singlet energy level below that of the triplet states with the splitting magnitude being Δ_{S-T} . The selection rules are shown in the diagram with the red/blue arrows denoting σ_{\pm} polarization.

Zeeman-splits the triplet states in energy to the states $|T_-\rangle_x$, $|T_0\rangle_x$ and $|T_+\rangle_x$ as shown in Fig. 4, while the modified singlet state, having no spin projection in the x direction, is not shifted in energy. The new triplet states are given by

$$|T_-\rangle_x = |-, -\rangle, \quad (18)$$

$$|T_0\rangle_x = 2^{-1/2}(|+, -\rangle + |-, +\rangle), \quad (19)$$

$$|T_+\rangle_x = |+, +\rangle, \quad (20)$$

where

$$|\pm\rangle = 2^{-1/2}(|\uparrow\rangle \pm |\downarrow\rangle) \quad (21)$$

are the eigenstates of the spin operator in x direction. The trion states are also Zeeman-split in energy, with the new states being $|t_{\pm}, \pm\rangle$ and $|t_{\pm}, \pm\rangle$ and where the states $|t_{\pm}\rangle$ are defined by

$$|t_{\pm}\rangle = 2^{-1/2}(|\downarrow\uparrow\uparrow\rangle \pm |\downarrow\uparrow\downarrow\rangle). \quad (22)$$

We plot the trion states Zeeman splittings in Fig. 4. With the energy levels determined, we write the selection rules for the Voigt geometry. We find the allowed transitions have linear polarizations in either the x or y directions, and that the set of transitions, shown in Fig. 4, makes Raman transitions possible between all pairs of spin states apart from the pair of $|T_-\rangle_x$ and $|T_+\rangle_x$, a point that will be important later when we tackle the problem of complete quantum control of the two-electron spin state.

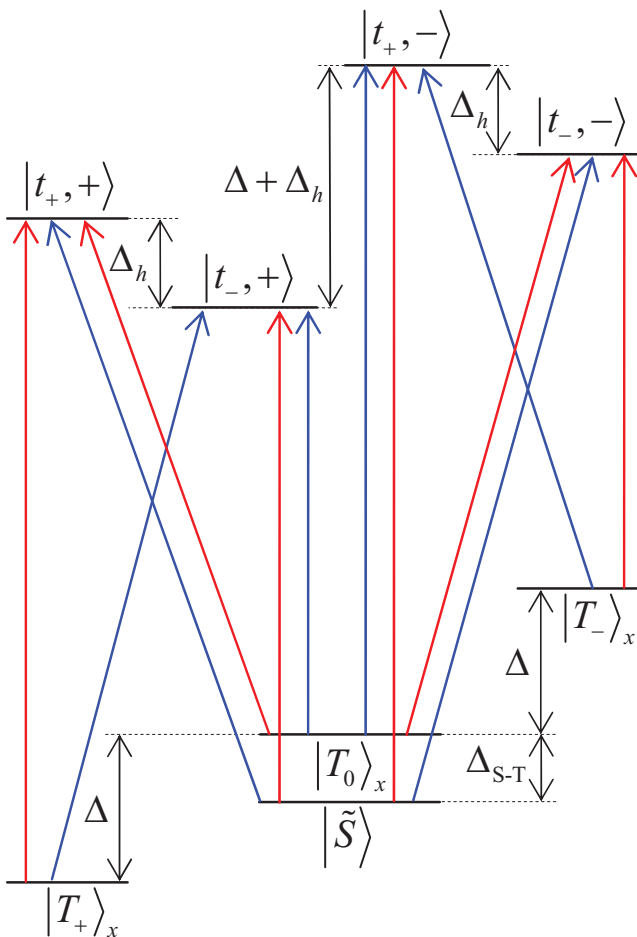


FIG. 4. (color online) Energy level diagram of the quantum dot molecule in the Voigt geometry (growth direction is z , and magnetic field is in $+x$ direction). The energy of the modified singlet state $|\tilde{S}\rangle$ is unaffected by the magnetic field and remains split from $|T_0\rangle_x$ by Δ_{S-T} , while the triplet states are Zeeman-split in energy to $|T_+\rangle_x$, $|T_0\rangle_x$ and $|T_-\rangle_x$, with the splitting being $\Delta = |g_e|\mu_B B$, g_e the electron g -factor, μ_B the Bohr magneton and B the magnitude of the magnetic field. The degeneracy of the optically excited states is also removed by the magnetic field and the states are Zeeman-split as shown in the figure, where $\Delta_h = |g_h|\mu_B B$ and g_h is the hole g -factor. The selection rules are plotted in the diagram with red arrows corresponding to V (π_y) polarization, and blue arrow arrows to H (π_x) polarization.

III. UNIVERSAL COMPUTATION WITH TWO-LEVEL OPERATIONS

The spin states in the quantum dot molecule system in the Voigt geometry form a basis for a two-qubit computational state space. This basis is $|\pm, \pm\rangle$, where the $|\pm\rangle$ states were defined in Eq. (21), and where the admixtures of the doubly-occupied states were omitted for brevity. The scheme for universal computation we propose provides a realization of a given arbitrary unitary operation in the computational basis through the appli-

cation of a set of two-level unitary operations between the spin states. Each of the two-level unitary operations operates on two spin levels and is realized through two laser pulses with the same Raman detuning δ that pump the transitions from the two spin states to a common trion state.

Suppose we want to realize a given a unitary operation U in the computational basis as a product of two-level unitary operations. A general proper unitary two-level operation in the space of the states $|i\rangle$ and $|j\rangle$ ($i, j = 1, \dots, 4$) in the spin state basis, $|\tilde{S}\rangle$, $|T_0\rangle_x$, $|T_+\rangle_x$ and $|T_-\rangle_x$, is given by

$$R_{ij}(\theta, \hat{n}) = \exp(-i\frac{\theta}{2}\hat{n} \cdot \boldsymbol{\sigma}), \quad (23)$$

which rotates the pseudo-spin vector in the subspace of the states $|i\rangle$ and $|j\rangle$ by an angle θ about the axis \hat{n} , with $\boldsymbol{\sigma} = (\sigma_x, \sigma_y, \sigma_z)$ acting in the subspace of these two levels. Going back to the unitary operation U , we first write its matrix relative to the spin state basis. Then, Ref. 38 shows how to decompose an arbitrary n -qubit unitary operation to a product of up to $\binom{2^n}{2}$ two-level unitary operations. However, we prefer the operations in the product to be proper unitary, as such operations are more easily implemented experimentally,⁴⁴ and we give in Appendix A the procedure for decomposing U to a product of up to 6 proper unitary two-level operators in the form of Eq. (23) and an overall phase factor, which can be omitted.

From the energy level diagram in Fig. 4 it can be seen that apart from R_{34} each of the 6 two-level unitary operators that may appear in the decomposition of U , namely R_{12} , R_{13} , R_{14} , R_{23} , R_{24} and R_{34} , may be implemented with a single Raman transition. A graphical illustration of the situation appears in the graph in Fig. 5, wherein each vertex represents a level and each edge a possible two-level unitary operation. The operation R_{34} may be implemented through 3 Raman transitions as shown by the following argument. If we represent a π rotation operation between the states $|i\rangle$ and $|j\rangle$ as

$$P_{ij} = R_{ij}(\pi, \hat{y}), \quad (24)$$

then we have

$$R_{ik} = P_{jk}R_{ij}P_{jk}^\dagger, \quad (25)$$

$$R_{kj} = P_{ik}R_{ij}P_{ik}^\dagger. \quad (26)$$

With the problem of R_{34} solved, we consider the fact that it may be advantageous to use of only some of the two-level unitary operations, as the realizations of those using Raman transitions may be faster or have higher fidelity relative to the other operations. We therefore ask what universal subsets of the 5 operations can be chosen, i.e. subsets with which any arbitrary unitary operation can be implemented. The answer to this question lies in the graph interpretation of Eqs. (25-26). These equations

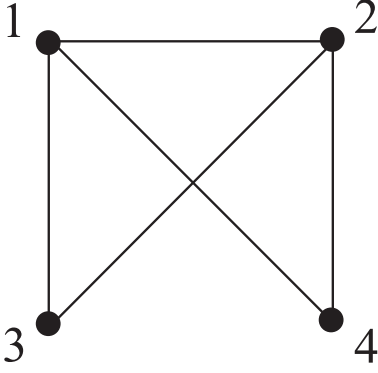


FIG. 5. Graph representation of the spin states and the possible two-level operations between them. The graph vertices represent levels and its edges represent possible two-level unitary operations. The vertices 1, 2, 3 and 4 are associated with the states $|\tilde{S}\rangle$, $|T_0\rangle_x$, $|T_+\rangle_x$ and $|T_-\rangle_x$, respectively.

show that an edge may be realized by 3 Raman transitions if a two-edge path connects its vertices. Extending

$$\mathcal{H} = \begin{pmatrix} -\Delta_{S-T} & 0 & 0 & 0 & \chi_H^* & -\chi_V^* & \chi_V^* & -\chi_H^* \\ 0 & 0 & 0 & 0 & \chi_V^* & -\chi_H^* & \chi_H^* & -\chi_V^* \\ 0 & 0 & -\Delta & 0 & \sqrt{2}\chi_V^* & 0 & \sqrt{2}\chi_H^* & 0 \\ 0 & 0 & 0 & \Delta & 0 & \sqrt{2}\chi_H^* & 0 & \sqrt{2}\chi_V^* \\ \chi_H & \chi_V & \sqrt{2}\chi_V & 0 & E_{tr} + (\Delta_h - \Delta)/2 & 0 & 0 & 0 \\ -\chi_V & -\chi_H & 0 & \sqrt{2}\chi_H & 0 & E_{tr} + (\Delta_h + \Delta)/2 & 0 & 0 \\ \chi_V & \chi_H & \sqrt{2}\chi_H & 0 & 0 & 0 & E_{tr} - (\Delta_h + \Delta)/2 & 0 \\ -\chi_H & -\chi_V & 0 & \sqrt{2}\chi_V & 0 & 0 & 0 & E_{tr} - (\Delta_h - \Delta)/2 \end{pmatrix}, \quad (27)$$

where E_{tr} is the trion state energy shown in Fig. 3, we have set $\hbar = 1$, $\Delta = |g_e|\mu_B B$ is the electron Zeeman splitting, $\Delta_h = |g_h|\mu_B B$ is the hole Zeeman splitting, and where μ_B is the Bohr magnetron, B is the magnetic field magnitude, and g_e and g_h are the electron and hole

$$\mathcal{H} = \begin{pmatrix} 0 & 0 & 0 & 0 & \chi_H^* e^{i\Delta_{15}t} & -\chi_V^* e^{i\Delta_{16}t} & \chi_V^* e^{i\Delta_{17}t} & -\chi_H^* e^{i\Delta_{18}t} \\ 0 & 0 & 0 & 0 & \chi_V^* e^{i\Delta_{25}t} & -\chi_H^* e^{i\Delta_{26}t} & \chi_H^* e^{i\Delta_{27}t} & -\chi_V^* e^{i\Delta_{28}t} \\ 0 & 0 & 0 & 0 & \sqrt{2}\chi_V^* e^{i\Delta_{35}t} & 0 & \sqrt{2}\chi_H^* e^{i\Delta_{37}t} & 0 \\ 0 & 0 & 0 & 0 & 0 & \sqrt{2}\chi_H^* e^{i\Delta_{46}t} & 0 & \sqrt{2}\chi_V^* e^{i\Delta_{48}t} \\ \chi_H e^{-i\Delta_{15}t} & \chi_V e^{-i\Delta_{25}t} & \sqrt{2}\chi_V e^{-i\Delta_{35}t} & 0 & 0 & 0 & 0 & 0 \\ -\chi_V e^{-i\Delta_{16}t} & -\chi_H e^{-i\Delta_{26}t} & 0 & \sqrt{2}\chi_H e^{-i\Delta_{46}t} & 0 & 0 & 0 & 0 \\ \chi_V e^{-i\Delta_{17}t} & \chi_H e^{-i\Delta_{27}t} & \sqrt{2}\chi_H e^{-i\Delta_{37}t} & 0 & 0 & 0 & 0 & 0 \\ -\chi_H e^{-i\Delta_{18}t} & -\chi_V e^{-i\Delta_{28}t} & 0 & \sqrt{2}\chi_V e^{-i\Delta_{48}t} & 0 & 0 & 0 & 0 \end{pmatrix}, \quad (28)$$

where $\Delta_{ij} = E_i - E_j$, and where E_i is the energy of the state $|i\rangle$. Eqs. (27) and (28) were derived with $|\tilde{S}\rangle$

this result by induction, we find that an edge can be realized by $2n - 1$ Raman transitions if a path of n edges connects its vertices. An important result follows. For a subset of the graph in Fig. 5 to be universal, it must include all vertices and be connected. When we define π -edges as edges representing $\pm\pi$ rotations, the graph for the minimal universal set of operations can be found and its form is given in App. B.

IV. PULSE SHAPING

The two-level unitary operations in our system are realized through Raman transitions. For such a transition to implement R_{ij} the quantum dot molecule is illuminated by two phase-locked laser pulses propagating in the z direction. The two pulses are linearly polarized, following the selection rules in Fig. 4, in either the vertical (V) or horizontal (H) directions, have a common Raman detuning δ and pump the two transitions from the spin states $|i\rangle$ and $|j\rangle$ to a common trion state. The model Hamiltonian in the basis of $|\tilde{S}\rangle$, $|T_0\rangle_x$, $|T_+\rangle_x$, $|T_-\rangle_x$, $|t_+, +\rangle$, $|t_+, -\rangle$, $|t_-, +\rangle$, and $|t_-, -\rangle$, in the rotating wave approximation (RWA) is

g -factors, respectively. The expressions $\chi_V(t) = \Omega_V(t)/2$ and $\chi_H(t) = \Omega_H(t)/2$ in Eq. (27) are, respectively, halves of the time-dependent Rabi frequency for the transitions $|\tilde{S}\rangle \rightarrow |t_-, +\rangle$ and $|T_0\rangle_x \rightarrow |t_-, +\rangle$.

In the interaction representation the Hamiltonian in Eq. (27) is recast as

approximated as the singlet state $|S\rangle$. When the full

expression for $|\tilde{S}\rangle$ is used, the Hamiltonian matrices are the same, apart from an extra numerical factor in the off-diagonal matrix elements involving $|\tilde{S}\rangle$. This factor is the coefficient of $|S\rangle$ in $|\tilde{S}\rangle$, which for the experimental values in Ref. 22 is 0.973.

As seen from the energy level diagram in Fig. 4, a Raman transition from one spin state to another may suffer from unintended dynamics due to the presence of close resonances. Rather than increase the pulses lengths, which will make the operation slower and magnify the effects of dephasing, we cope with the unintended dynamics through pulse shaping,^{44,45} whereby we vary the parameters of the pulses to optimize the operation.

We describe the explicit form of $\chi_V(t)$ and $\chi_H(t)$ with pulse shaping for the V-H, H-H and V-V cases, with the case names denoting the polarizations of the Raman laser pulses involved. In the V-H case we have

$$\chi_V(t) = \chi_0(t) + \tilde{\chi}_2(t), \quad (29)$$

$$\chi_H(t) = \chi_1(t - \Delta t) + \tilde{\chi}_3(t - \Delta t), \quad (30)$$

where

$$\chi_j(t) = \chi_j e^{-(t/\tau_j)^2} e^{-i\omega_j t + i\varphi_j}, \quad (31)$$

$$\tilde{\chi}_j(t) = \chi_j(t) e^{i\varphi'_j \ln \cosh(t/\tau_j)}, \quad (32)$$

and where $\chi_j(t)$ ($j = 0, 1$) is a main pulse with amplitude χ_j , pulse width τ_j , central frequency ω_j and constant phase φ_j . The shift in time between the two main pulses is given by Δt . The expression $\tilde{\chi}_j(t)$ ($j = 2, 3$) in Eq. (32) is a helping pulse designed to alleviate the effects of unintended dynamics. This pulse has an additional chirping term,⁴⁶ which sweeps the instantaneous frequency in time through a range of frequencies centered about ω_j .

The pulse shapes for the other two cases involve only one polarization type. In the H-H case we have

$$\chi_V(t) = 0, \quad (33)$$

$$\begin{aligned} \chi_H(t) &= \chi_0(t) + \tilde{\chi}_2(t) + \\ &\quad \chi_1(t - \Delta t) + \tilde{\chi}_3(t - \Delta t), \end{aligned} \quad (34)$$

and in the V-V case we have

$$\begin{aligned} \chi_V(t) &= \chi_0(t) + \tilde{\chi}_2(t) + \\ &\quad \chi_1(t - \Delta t) + \tilde{\chi}_3(t - \Delta t), \end{aligned} \quad (35)$$

$$\chi_H(t) = 0. \quad (36)$$

The pulse parameters should be varied so as to maximize the fidelity of the operation relative to the ideal R_{ij} . As this fidelity depends on the input state, the expected value of the fidelity over all possible input states is required. Let the states in the basis $|\tilde{S}\rangle$, $|T_0\rangle_x$, $|T_+\rangle_x$, $|T_-\rangle_x$, $|t_+, +\rangle$, $|t_+, -\rangle$, $|t_-, +\rangle$, and $|t_-, -\rangle$ be denoted by $|j\rangle$ ($j = 1, \dots, 8$). For unitary evolution we find in App. C the expected fidelity is

$$\bar{F} = \frac{1}{20} \sum_{i=1}^4 \sum_{j=1}^4 (I_{ii} I_{jj}^* + |I_{ij}|^2), \quad (37)$$

where

$$I_{ij} = \langle i | \tilde{U}^\dagger U_{id} | j \rangle, \quad (38)$$

and where \tilde{U} and U_{id} are, respectively, the actual and ideal evolution operators. The expected fidelity in Eq. (37) is the yardstick by which we decide whether one set of pulse parameters is better than another set of parameters for the implementation of a given two-level unitary operation R_{ij} .

We now incorporate the effects of light hole mixing in our analysis. The hole states $|\uparrow\rangle$ and $|\downarrow\rangle$ in Eq. (22), denoted as $|H_z^\pm\rangle$, and heretofore taken as bare heavy hole states, are better approximated through the Luttinger Hamiltonian^{47,48} as a superposition of heavy hole states and light hole states of the form

$$|H_z^\pm\rangle = \cos \theta_m \left| \frac{3}{2}, \pm \frac{3}{2} \right\rangle - \sin \theta_m e^{\mp i\phi_m} \left| \frac{3}{2}, \mp \frac{1}{2} \right\rangle. \quad (39)$$

In Eq. (39) θ_m and ϕ_m are the mixing angles, $|\frac{3}{2}, \pm \frac{3}{2}\rangle$ are the heavy hole states, $|\frac{3}{2}, \pm \frac{1}{2}\rangle$ the light hole states, and the quantization axis is taken as the growth direction (z direction).

When the new hole states in Eq. (39) are substituted in the trion states and the Hamiltonian matrix is calculated following an analogous derivation in the single dot case in Ref. 8, we find results identical with the ones obtained in this reference, namely that adjusting the polarizations of the lasers from \mathbf{V} and \mathbf{H} to $\mathbf{V}' = 2^{-1/2}(\boldsymbol{\sigma}_+ + e^{i\mu} \boldsymbol{\sigma}_-)$ and $\mathbf{H}' = 2^{-1/2}(\boldsymbol{\sigma}_+ - e^{-i\mu} \boldsymbol{\sigma}_-)$, with

$$e^{i\mu_\pm} = \frac{\sqrt{3} \cos \theta_m \pm \sin \theta_m e^{\pm i\phi_m}}{\sqrt{3} \cos \theta_m \pm \sin \theta_m e^{\mp i\phi_m}}, \quad (40)$$

the Hamiltonian has the same form as in the case with no light hole mixing [Eq. (28)] apart from replacing χ_V and χ_H by

$$\tilde{\chi}_{V'} = \chi_{V'} \frac{1 + 2 \cos 2\theta_m}{3 \cos \theta_m + \sqrt{3} e^{-i\phi_m} \sin \theta_m}, \quad (41)$$

$$\tilde{\chi}_{H'} = \chi_{H'} \frac{1 + 2 \cos 2\theta_m}{3 \cos \theta_m - \sqrt{3} e^{i\phi_m} \sin \theta_m}, \quad (42)$$

where $\chi_{V'}$ and $\chi_{H'}$ are the analogous quantities to χ_V and χ_H for light with V' and H' polarizations, respectively, and the effects of \mathbf{V}' and \mathbf{H}' being non-orthogonal are neglected.

The identity of the last results with the single dot case in Ref. 8 is not surprising, as only the bottom quantum dot is optically excited. To summarize, the effects of light holes mixing can be circumvented by adjusting the polarization of the laser pulses and their Rabi frequencies as noted above. With these adjustments, the Hamiltonian in Eq. (28) can still be used.

V. DECAY AND DECOHERENCE

When decay and decoherence are taken into account the state of the system may be described by a density

matrix ρ and its non-unitary evolution by a quantum master equation in the Lindblad form

$$\dot{\rho} = -i[\mathcal{H}, \rho] + \sum_i \mathcal{L}_i[\rho], \quad (43)$$

where H is given in Eq. (28), and where the sum is over all trion state relaxation channels, each of which is described by a Lindblad superoperator

$$\mathcal{L}_i[\rho] = D_i \rho D_i^\dagger - \frac{1}{2} D_i^\dagger D_i \rho - \frac{1}{2} \rho D_i^\dagger D_i. \quad (44)$$

In taking the relaxation channels as separate and incoherent, we neglected spontaneously generated coherence (SGC), since we assumed the Zeeman splittings are large enough to satisfy $|\Delta_{jk}| \gg \Gamma$ ($j, k = 5, \dots, 8; j \neq k$), where Γ is the total relaxation rate of a given trion level,^{49,50} and that the level splittings Δ , Δ_h and Δ_{S-T} are larger or of the same order as the Rabi frequency Ω .⁵¹ The effects of pure dephasing are not included in Eq. (43), as this process, which is generated by the nuclear spins, has a rate much lower than the total trion dephasing rate in this system.^{9,52}

The 12 jump operators, D_i , in Eq. (43), each corresponding to a possible relaxation channel, are

$$D_1 = \sqrt{\Gamma/4} |\tilde{S}\rangle \langle t_+, +|, \quad (45)$$

$$D_2 = \sqrt{\Gamma/4} |T_0\rangle_x \langle t_+, +|, \quad (46)$$

$$D_3 = \sqrt{\Gamma/2} |T_+\rangle_x \langle t_+, +|, \quad (47)$$

$$D_4 = \sqrt{\Gamma/4} |\tilde{S}\rangle \langle t_+, -|, \quad (48)$$

$$D_5 = \sqrt{\Gamma/4} |T_0\rangle_x \langle t_+, -|, \quad (49)$$

$$D_6 = \sqrt{\Gamma/2} |T_-\rangle_x \langle t_+, -|, \quad (50)$$

$$D_7 = \sqrt{\Gamma/4} |\tilde{S}\rangle \langle t_-, +|, \quad (51)$$

$$D_8 = \sqrt{\Gamma/4} |T_0\rangle_x \langle t_-, +|, \quad (52)$$

$$D_9 = \sqrt{\Gamma/2} |T_+\rangle_x \langle t_-, +|, \quad (53)$$

$$D_{10} = \sqrt{\Gamma/4} |\tilde{S}\rangle \langle t_-, -|, \quad (54)$$

$$D_{11} = \sqrt{\Gamma/4} |T_0\rangle_x \langle t_-, -|, \quad (55)$$

$$D_{12} = \sqrt{\Gamma/2} |T_-\rangle_x \langle t_-, -|. \quad (56)$$

The terms in the square roots in Eqs. (45-56) are the relaxation rates for the corresponding decay channels. These rates were determined by splitting the total decay rate, the trion state linewidth Γ , in the ratio of absolute square values of the dipole matrix elements for the allowed transitions from the this state to the spin states, as these values are proportional to the spontaneous decay rates of the corresponding channels.

With spontaneous decay and decoherence included in the model, the expression for the expected fidelity of an operation relative an ideal operation in Eq. (37) should be generalized. The derivation in App. D gives this generalized expected fidelity as

$$\overline{\mathcal{F}} = \frac{1}{20} \sum_{i=1}^4 \sum_{j=1}^4 \left[\langle j | U_{id}^\dagger \rho^{(ji)} U_{id} | i \rangle + \langle j | U_{id}^\dagger \rho^{(ii)} U_{id} | j \rangle \right], \quad (57)$$

where $\rho^{(ij)}$ is the density matrix resulting from the non-unitary evolution of an initial density matrix $|i\rangle\langle j|$. In the limit of unitary evolution ($\Gamma = 0$), $\rho^{(ij)} = \tilde{U} |i\rangle\langle j| \tilde{U}^\dagger$ and Eq. (57) reduces to Eq. (37).

VI. THE TWO-QUBIT QUANTUM FOURIER TRANSFORM

As a case in point of a non-trivial two-qubit transformation realized using the methods described above, we choose the two-qubit quantum Fourier transformation. In the computational basis $|\pm, \pm\rangle$ this transformation is

$$U_{QFT} = \frac{1}{2} \begin{pmatrix} 1 & 1 & 1 & 1 \\ 1 & i & -1 & -i \\ 1 & -1 & 1 & -1 \\ 1 & -i & -1 & i \end{pmatrix}. \quad (58)$$

Rewriting Eq. (58) relative to the physical basis $|\tilde{S}\rangle$, $|T_0\rangle_x$, $|T_+\rangle_x$, and $|T_-\rangle_x$ as \tilde{U}_{QFT} , and applying the algorithm in App. A to decompose the result to a product of two-level proper unitary operations, we find

$$\tilde{U}_{QFT} = e^{i\alpha} R_{32}(\theta_{32}, \hat{n}_{32}) R_{34}(\theta_{34}, \hat{n}_{34}) R_{12}(\theta_{12}, \hat{n}_{12}) \times R_{14}(\theta_{14}, \hat{n}_{14}) R_{24}(\theta_{24}, \hat{n}_{24}), \quad (59)$$

where $R_{ij}(\theta, \hat{n})$ is defined in Eq. (23), and where α , θ_{ij} and \hat{n}_{ij} were numerically determined.

We detail the optimization process of the pulse train. First, we choose the physical parameters for the system as the ones in Ref. 22, namely $h_B = 2.6$ nm, $h_T = 3.2$ nm, $d_0 = 9$ nm (see Fig. 1) and $\Delta_{S-T} = 125$ μ eV. The electron and hole g -factors are taken from Ref. 6 as $g_e = -0.48$ and $g_h = 0.31$, and the trion states linewidth Γ is obtained from Ref. 4 as $\Gamma = 1.2$ μ eV. Next, for each of the operations R_{12} , R_{13} , R_{14} , R_{23} and R_{24} we choose the trion state that will be used to realize the Raman transition. We choose this state so as to reduce the unintended dynamics, i.e. such that the resonance frequencies of each of the transitions from the two spin states to this trion state is as far as possible from other allowed transitions with the same polarization. We then choose a value for the magnetic field B that maximizes the minimum absolute frequency difference among all pairs of allowed transitions with the same polarization. For magnetic field values lower than 10 T, this value is found to be $B = 8.99$ T, and the minimum absolute frequency difference is 36.5 μ eV.

We then turn to the optimization of the individual pulses. Since each R_{ij} in Eq. (59) (apart from R_{34}) can be implemented directly as given or indirectly via Eqs. (25-26), we consider all possible indirect implementations and optimize the 35 operations $R_{ij}(\theta_{32}, \hat{n}_{32})$, $R_{ij}(\theta_{34}, \hat{n}_{34})$, $R_{ij}(\theta_{12}, \hat{n}_{12})$, $R_{ij}(\theta_{14}, \hat{n}_{14})$, $R_{ij}(\theta_{24}, \hat{n}_{24})$, P_{ij} and P_{ij}^\dagger , where $(i, j) = (1, 2), (1, 3), (1, 4), (2, 3), (2, 4)$. In each optimization we realize the operation with two main pulses, each of which having the form of Eq. (31), and maximize

the expected fidelity in Eq. (37) through grid search in pulse parameter space followed by gradient descent. In the optimization process we keep in mind the need for short pulses that will ensure fast operation. Examining the results of the optimizations, we conclude that direct implementation is always preferable when possible, with the only case where indirect implementation is chosen being

$$R_{34}(\theta_{34}, \hat{n}_{34}) = P_{13}R_{14}(\theta_{34}, \hat{n}_{34})P_{13}^\dagger, \quad (60)$$

which cannot be directly implemented due to the selection rules.

With the pulse train determined to consist of 7 operations, we add two helping pulses, each in the form of Eq. (32), to each operation. The parameters of the first helping pulse are varied so as to maximize the fidelity in Eq. (37) and the process is repeated for the second helping pulse. Following the optimization of the helping pulses, we turn to the optimization of the time spacings between the 7 operations. The fidelity we maximize is now the fidelity of the entire QFT with decay and decoherence taken into account as given in Eq. (57). The resulting optimized pulse trains are calculated to have an expected fidelity of 84.9% and a duration of 453 ps when helping pulses are not employed, and an expected fidelity of 88.1% and a duration of 414 ps when helping pulses are used. The main source of the infidelity is unintended dynamics, that is excitation of levels other than the ones intended. This result is revealed comparing the fidelities in Eq. (37) and Eq. (57) for each of the individual operations. We find the decrease in fidelity from unity due to decoherence and decay is, on average, 0.8% per operation, while the decrease due to unintended dynamics is 2.6% per operation. This result could have been expected as the minimum absolute frequency difference of 36.5 μeV is always comparable to or smaller than the spectral width of the pulses.

VII. CONCLUSIONS

In this work, we demonstrated a scheme for complete quantum control of a system of two singly-charged QDs coupled by coherent electron tunneling. We derived the energy level diagram for the system and chose the two-level operations realized by the 5 possible Raman transitions through the trion states as the universal set of gates. In contrast with the commonly used universal computation scheme of CNOT gates and single-qubit gates,³⁹ we used only two-qubit gates, each realizable through a few laser pulses. Our choice is advantageous as single-qubit gates, which can be described as two simultaneous two-qubit gates, tend to suffer from unintended dynamics in this system.²² We demonstrated our scheme by describing the realization of the two-qubit QFT in the QDM system with a reasonably high fidelity of 88.1%. We incorporated light hole mixing, decay and decoherence in our analysis.

Our results indicate that pulse shaping can substantially increase the fidelity of quantum operations in optically active QDs, and that the QDM is a promising platform for multi-qubit quantum computation. The main limitations for increasing the overall fidelity of a given two-qubit operation with this scheme are unintended dynamics, decay and decoherence. The first can be dealt with through improved pulse shaping. Due to limited computing power, we chose our pulse search algorithm to optimize each pulse separately. A better optimization may be achieved through simultaneous optimization of all 4 pulses of a given operation. Ameliorating the effects of decoherence and decay can also be achieved by improved pulse search methods. In our search we maximized the fidelity expression in Eq. (37) that does not take decay and decoherence into account, rather than the expression that takes these effects into account in Eq. (57). Using the latter expression, which takes much longer to evaluate, will increase the fidelity of the overall operation.

The experimental realization of universal computation in QDMs will be a major step towards building a QD-based optically-controlled quantum computer. Future research may look into methods for robust and effective entanglement generation between distant QDMs, possibly with multi-photon light, as was suggested for single QDs.^{53,54} Quantum computations with more than two qubits may be realized in a quantum network of entangled QDMs through unitary operations on each of the QDMs, possibly employing the theory of cluster states.⁵⁵

Appendix A: Decomposition of a Unitary Operation to a Product of Two-Level Proper Unitary Operations

In this appendix we show a procedure to decompose a given unitary operation U to a product of an overall phase factor $e^{i\alpha}$ and two-level proper unitary operations. The procedure is given for the case of a 3-state basis, but can be easily extended to an N -state basis with $N > 3$.

The first step in the algorithm is to factor out $|U| = e^{i\alpha}$ and proceed with $U' = e^{-i\alpha/3}U$, which is proper unitary. Let U' be given by

$$U' = \begin{pmatrix} a & d & g \\ b & e & h \\ c & f & g \end{pmatrix}. \quad (A1)$$

If $b = 0$, we take U_1 as the identity matrix and proceed to the next step. Otherwise we take U_1 as the proper unitary matrix

$$U_1 = \frac{1}{\sqrt{|a|^2 + |b|^2}} \begin{pmatrix} a^* & b^* & 0 \\ -b & a & 0 \\ 0 & 0 & 1 \end{pmatrix} \quad (A2)$$

and have

$$U_1 U' = \begin{pmatrix} a' & d' & g' \\ 0 & e' & h' \\ c' & f' & j' \end{pmatrix}. \quad (A3)$$

Then, if $c' = 0$, we take U_2 as the identity matrix and proceed to the next step, while if $c' \neq 0$, we define

$$U_2 = \frac{1}{\sqrt{|a'|^2 + |c'|^2}} \begin{pmatrix} a'^* & 0 & c'^* \\ 0 & 1 & 0 \\ -c' & 0 & a' \end{pmatrix}, \quad (\text{A4})$$

which is proper unitary, and have

$$U_2 U_1 U' = \begin{pmatrix} 1 & 0 & 0 \\ 0 & e'' & h'' \\ 0 & f'' & j'' \end{pmatrix} \equiv U_3. \quad (\text{A5})$$

Hence, the sought decomposition is

$$U = |U|^{1/3} U_1^{-1} U_2^{-1} U_3. \quad (\text{A6})$$

Appendix B: The Minimal Universal Set of Operations in the Quantum Dot Molecule

In this appendix, we prove the minimal universal set of two-level unitary operations in the quantum dot molecule system is represented by the graph in Fig. 6. In the last paragraph of Sec. III it was shown that a graph representing a universal set of operations must be connected and contain all vertices. Hence, the minimum number of edges is 3. The edges cannot all be π edges since then the number of possible two-qubit unitary operations attainable with a finite number of such two-level operations is finite. We conclude the set of operations represented by the graph in Fig. 6 is minimal.

This set of operations is universal, since each of the 6 two-level unitary operations that can appear in the decomposition of an arbitrary unitary operation U can be written in terms of the 3 operations in the set through use of Eqs. (25-26), namely

$$R_{12} = R_{12}, \quad (\text{B1})$$

$$R_{13} = P_{23} R_{12} P_{23}^\dagger, \quad (\text{B2})$$

$$R_{14} = P_{21} P_{14} R_{21} P_{14}^\dagger P_{21}^\dagger, \quad (\text{B3})$$

$$R_{23} = P_{12} P_{23} R_{12} P_{23}^\dagger P_{12}^\dagger, \quad (\text{B4})$$

$$R_{24} = P_{14} R_{21} P_{14}^\dagger, \quad (\text{B5})$$

$$R_{34} = P_{14} P_{23} R_{21} P_{23}^\dagger P_{14}^\dagger, \quad (\text{B6})$$

with R_{ij} and P_{ij} defined in Eq. (23) and Eq. (24), respectively.

Appendix C: The Expected Fidelity for Unitary Evolution

In this appendix, we derive the expression for the expected fidelity of an operation relative to an ideal operation when state evolution is unitary. The input state $|\psi_{in}\rangle$ is given by

$$|\psi_{in}\rangle = \sum_{j=1}^4 b_j |j\rangle, \quad (\text{C1})$$

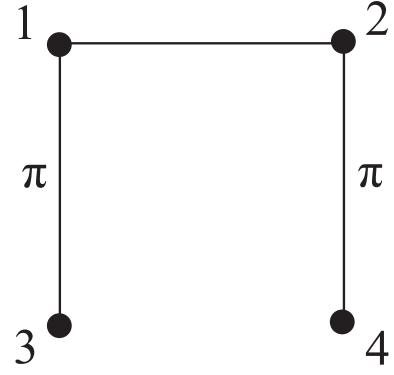


FIG. 6. Graph representation of the minimal subset of the possible two-level operations that can still achieve universal computation. The graph vertices represent levels and its edges represent possible two-level unitary operations. A π -edge represents a $\pm\pi$ rotation operation. The vertices 1, 2, 3 and 4 are associated with the states $|\tilde{S}\rangle$, $|T_0\rangle_x$, $|T_+\rangle_x$ and $|T_-\rangle_x$, respectively.

while the output state is

$$|\psi_{out}\rangle = \tilde{U}|\psi_{in}\rangle = \sum_{j=1}^8 c_j |j\rangle, \quad (\text{C2})$$

with \tilde{U} being the evolution operator. The ideal output state is given by

$$|\psi_{id}\rangle = U_{id}|\psi_{in}\rangle = \sum_{j=1}^4 d_j |j\rangle, \quad (\text{C3})$$

where U_{id} is the ideal evolution operator. The fidelity of the output state relative to the ideal output state is calculated as

$$\mathcal{F} = \langle \psi_{id} | \text{Tr}_T(|\psi_{out}\rangle\langle\psi_{out}|) | \psi_{id} \rangle, \quad (\text{C4})$$

where we trace over the trion states. Plugging Eqs. (C2) and (C3) in Eq. (C4), we find

$$\mathcal{F} = \left| \sum_{j=1}^4 c_j^* d_j \right|^2. \quad (\text{C5})$$

Averaging Eq. (C5) over all possible input states as in Ref. 44, the expected fidelity of the operation is obtained in the form of Eq. (37).

Appendix D: The Expected Fidelity for Non-Unitary Evolution

In this appendix, we derive the expected fidelity of an operation relative to an ideal operation when state evolution is non-unitary. Let the initial state be a pure

state $|\psi_{in}\rangle$. This state evolves to the density matrix ρ with the evolution written in terms of effect operators A_k as

$$\rho = \sum_{k=1}^{N_1} A_k |\psi_{in}\rangle \langle \psi_{in} | A_k^\dagger. \quad (\text{D1})$$

The fidelity of ρ in Eq. (D1) relative to an ideally evolved state $|\psi_{id}\rangle = U_{id}|\psi_{in}\rangle$ is given by

$$\mathcal{F} = \sum_{k=1}^{N_1} |\langle \psi_{in} | A_k^\dagger U_{id} | \psi_{in} \rangle|^2. \quad (\text{D2})$$

When each term in Eq. (D2) is averaged over all possible input states, we find, using Eqs. (37-38), the expected fidelity is

$$\overline{\mathcal{F}} = \frac{1}{20} \sum_{k=1}^{N_1} \sum_{i=1}^4 \sum_{j=1}^4 \left(I_{ii}^{(k)} I_{jj}^{(k)} + |I_{ij}^{(k)}|^2 \right), \quad (\text{D3})$$

where $I_{ij}^{(k)} = \langle i | A_k^\dagger U_{id} | j \rangle$. Changing the order of summation in Eq. (D3) and using Eq. (D1) for the time evolution, we obtain Eq. (57).

ACKNOWLEDGMENTS

This research was supported by U.S. Army Research Office MURI Award No. W911NF0910406, by NSF Grant No. PHY-1104446 and by ARO (IARPA, W911NF-08-1-0487). The authors thank L. J. Sham for helpful discussions.

REFERENCES

-
- ¹ Y. Yamamoto, T. D. Ladd, D. Press, S. Clark, K. Sanaka, C. Santori, D. Fattal, K. M. Fu, S. Höfling, S. Reitzenstein, and A. Forchel, *Phys. Scr.* **T137**, 014010 (2009)
 - ² R.-B. Liu, W. Yao, and L. J. Sham, *Adv. in Phys.* **59**, 703 (2010)
 - ³ D. P. DiVincenzo, *Fortschr. Phys.* **48**, 771 (2000)
 - ⁴ M. Atatüre, J. Dreiser, A. Badolato, A. Högele, K. Karrai, and A. Imamoglu, *Science* **312**, 551 (2006)
 - ⁵ C. Emary, X. Xu, D. G. Steel, S. Saikin, and L. J. Sham, *Phys. Rev. Lett.* **98**, 047401 (2007)
 - ⁶ X. Xu, Y. Wu, B. Sun, Q. Huang, J. Cheng, D. G. Steel, A. S. Bracker, D. Gammon, C. Emary, and L. J. Sham, *Phys. Rev. Lett.* **99**, 097401 (2007)
 - ⁷ X. Xu, B. Sun, P. R. Berman, D. G. Steel, A. S. Bracker, D. Gammon, and L. J. Sham, *Nat. Phys.* **4**, 692 (2008)
 - ⁸ C. Emary and L. J. Sham, *J. Phys.: Condens. Matter* **19**, 056203 (2007)
 - ⁹ J. R. Schaibley, A. P. Burgers, G. A. McCracken, D. G. Steel, A. S. Bracker, D. Gammon, and L. J. Sham, *Phys. Rev. B* **87**, 115311 (2013)
 - ¹⁰ M. Atatüre, J. Dreiser, A. Badolato, and A. Imamoglu, *Nat. Phys.* **3**, 101 (2007)
 - ¹¹ A. N. Vamivakas, C.-Y. Lu, C. Matthiesen, Y. Zhao, S. Fält, A. Badolato, and M. Atatüre, *Nat. Lett.* **467**, 297 (2010)
 - ¹² C. Schneider, M. Strauß, T. Sünner, A. Huggenberger, D. Wiener, S. Reitzenstein, M. Kamp, S. Höfling, and A. Forchel, *Appl. Phys. Lett.* **92**, 183101 (2008)
 - ¹³ M. Winger, A. Badolato, K. J. Hennessy, E. L. Hu, and A. Imamoglu, *Phys. Rev. Lett.* **101**, 226808 (2008)
 - ¹⁴ P. Gallo, M. Felici, B. Dwir, K. A. Atlasov, K. F. Karlsson, A. Rudra, A. Mohan, G. Biasiol, L. Sorba, and E. Kapon, *Appl. Phys. Lett.* **92**, 263101 (2008)
 - ¹⁵ S. G. Carter, T. M. Sweeney, M. Kim, C. S. Kim, D. Solenov, S. E. Economou, T. L. Reinecke, L. Yang, A. S. Bracker, and D. Gammon, *Nat. Photonics* **7**, 329334 (2013)
 - ¹⁶ M. Pelton, C. Santori, J. Vučković, B. Zhang, G. S. Solomon, J. Plant, and Y. Yamamoto, *Phys. Rev. Lett.* **89**, 233602 (2002)
 - ¹⁷ E. Moreau, I. Robert, L. Manin, V. Thierry-Mieg, J. M. Gérard, and I. Abram, *Physica E* **13**, 418 (2002)
 - ¹⁸ A. Greulich, S. E. Economou, S. Spatzek, D. R. Yakovlev, D. Reuter, A. D. Wieck, T. L. Reinecke, and M. Bayer, *Nat. Phys.* **5**, 262 (2009)
 - ¹⁹ E. D. Kim, K. Truex, X. Xu, B. Sun, D. G. Steel, A. S. Bracker, D. Gammon, and L. J. Sham, *Phys. Rev. Lett.* **104**, 167401 (2010)
 - ²⁰ L.-B. Chen, L. J. Sham, and E. Waks, *Phys. Rev. B* **85**, 115319 (2012)
 - ²¹ D. Solenov, S. E. Economou, and T. L. Reinecke, *Phys. Rev. B* **87**, 035308 (2013)
 - ²² D. Kim, S. G. Carter, A. Greulich, A. S. Bracker, and D. Gammon, *Nat. Phys.* **7**, 223 (2010)
 - ²³ W. B. Gao, P. Fallahi, E. Togan, J. Miguel-Sanchez, and A. Imamoglu, *Nature (London)* **491**, 426 (2012)
 - ²⁴ J. R. Schaibley, A. P. Burgers, G. A. McCracken, L.-M. Duan, P. R. Berman, D. G. Steel, A. S. Bracker, D. Gammon, and L. J. Sham, *Phys. Rev. Lett.* **110**, 167401 (2013)
 - ²⁵ L. A. Webster, K. Truex, L.-M. Duan, D. G. Steel, A. S. Bracker, D. Gammon, and L. J. Sham, *Phys. Rev. Lett.* **112**, 126801 (2014)
 - ²⁶ D. Press, K. De Greve, P. L. McMahon, T. D. Ladd, B. Friess, C. Schneider, M. Kamp, S. Höfling, A. Forchel, and Y. Yamamoto, *Nat. Photonics Lett.* **4**, 367 (2010)
 - ²⁷ B. Sun, C. M. Eam Chow, D. G. Steel, A. S. Bracker, D. Gammon, and L. J. Sham, *Phys. Rev. Lett.* **108**, 187401 (2012)
 - ²⁸ M. F. Doty, M. Scheibner, A. S. Bracker, I. V. Ponomarev, T. L. Reinecke, and D. Gammon, *Phys. Rev. B* **78**, 115316 (2008)
 - ²⁹ M. Scheibner, A. S. Bracker, D. Kim, and Gammon, *Solid State Communications* **149**, 1427 (2009)
 - ³⁰ D. Kim, S. E. Economou, S. C. Bădescu, M. Scheibner, A. S. Bracker, M. Bashkansky, T. L. Reinecke, and

- D. Gammon, Phys. Rev. Lett. **101**, 236804 (2008)
- ³¹ C. Emary and L. J. Sham, Phys. Rev. B **75**, 125317 (2007)
- ³² L. Robledo, J. Elzerman, G. Jundt, M. Atatüre, A. Högele, S. Fält, and A. Imamoglu, Science **320**, 772 (2008)
- ³³ S. E. Economou and T. L. Reinecke, Phys. Rev. B **78**, 115306 (2008)
- ³⁴ J. I. Climente, M. Korkusinski, G. Goldoni, and P. Hawrylak, Phys. Rev. B **78**, 115323 (2008)
- ³⁵ H. J. Krenner, M. Sabathil, E. C. Clark, A. Kress, D. Schuh, M. Bichler, G. Abstreiter, and J. J. Finley, Phys. Rev. Lett. **94**, 057402 (2005)
- ³⁶ G. Ortner, M. Bayer, Y. Lyanda-Geller, T. L. Reinecke, A. Kress, J. P. Reithmaier, and A. Forchel, Phys. Rev. Lett. **94**, 157401 (2005)
- ³⁷ M. F. Doty, J. I. Climente, M. Korkusinski, M. Scheibner, A. S. Bracker, P. Hawrylak, and D. Gammon, Phys. Rev. Lett. **102**, 047401 (2009)
- ³⁸ M. Reck, A. Zeilinger, H. J. Bernstein, and P. Bertani, Phys. Rev. Lett. **73**, 58 (1994)
- ³⁹ A. Barenco, C. H. Bennett, R. Cleve, D. P. DiVincenzo, N. Margolus, P. Shor, T. Sleator, J. A. Smolin, and H. Weinfurter, Phys. Rev. A **52**, 3457 (1995)
- ⁴⁰ D. P. DiVincenzo, Phys. Rev. A **51**, 1015 (1995)
- ⁴¹ A. Barenco, Proc. R. Soc. London Ser. A **449**, 678 (1995)
- ⁴² S. Lloyd, Phys. Rev. Lett. **75**, 346 (1995)
- ⁴³ D. Deutsch, A. Barenco, and A. Ekert, Proc. R. Soc. London Ser. A. **449**, 669 (1995)
- ⁴⁴ C. Piermarocchi, P. Chen, , Y. S. Dale, and L. J. Sham, Phys. Rev. B **65**, 075307 (2002)
- ⁴⁵ P. Chen, C. Piermarocchi, and L. J. Sham, Phys. Rev. Lett. **87**, 067401 (2001)
- ⁴⁶ R.-B. Liu, W. Yao, and L. J. Sham, Phys. Rev. B **72**, 081306(R) (2005)
- ⁴⁷ J. M. Luttinger and W. Kohn, Phys. Rev. **97**, 869 (1955)
- ⁴⁸ D. A. Broido and L. J. Sham, Phys. Rev. A **31**, 888 (1985)
- ⁴⁹ S. E. Economou, R.-B. Liu, L. J. Sham, and D. G. Steel, Phys. Rev. B **71**, 195327 (2005)
- ⁵⁰ H.-P. Breuer and F. Petruccione, *The Theory of Open Quantum Systems*, 1st ed. (Oxford University Press, 2002)
- ⁵¹ P. R. Berman and V. S. Malinovsky, *Principles of Laser Spectroscopy and Quantum Optics*, 90th ed. (2011)
- ⁵² S. M. Ulrich, S. Ates, S. Reitzenstein, A. Löffler, A. Forchel, and P. Michler, Phys. Rev. Lett. **106**, 247402 (2011)
- ⁵³ C.-K. Chan and L. J. Sham, Phys. Rev. Lett. **110**, 070501 (2013)
- ⁵⁴ G. Z. Cohen and L. J. Sham, Phys. Rev. B **88**, 245306 (2013)
- ⁵⁵ R. Raussendorf, D. E. Browne, and H. J. Briegel, Phys. Rev. A **68**, 022312 (2003)